I&EC research
Industrial & Engineering Chemistry Research

pubs.acs.org/IECR

Article

A Velocity Coupling Method for Atomization Modeling: Application to Piezoelectric Pulsation-Driven Glass Nozzles

Jinping Zha, Liangchao Shang, Winston Duo Wu, Xiao Dong Chen, and Jie Xiao*

Cite This: *Ind. Eng. Chem. Res.* 2024, 63, 16915−16927

Read Online

ACCESS | Metrics & More | Article Recommendations | Supporting Information

ABSTRACT: A velocity coupling method is presented for numerical investigation of droplet formation through glass nozzles driven by piezoelectric pulsation. The key idea is to first model the phenomena inside and outside of the nozzle separately. This approach allows in-nozzle and out-nozzle models to focus on their respective modeling challenges, e.g., coupled multiphysics beyond fluid mechanics for the former and liquid−air interface tracking for the latter. After coupling them through velocity mapping, the complete atomization process can be simulated. The results show that periodic pulsation of the piezoceramic component attached to the glass capillary drives regular displacement of the capillary wall, leading to a rhythmic change in the chamber volume and hence the flow rate ejected from the nozzle. Such disturbance results in the breakup of a liquid jet into a stream of droplets. To demonstrate model effectiveness, the impact of disturbance frequency on atomization has been analyzed.

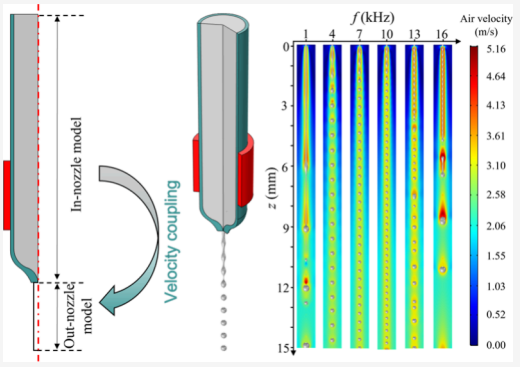

1. INTRODUCTION

Atomization is the process of generating tiny droplets by breaking up liquid jets or sheets,[1] which are ejected from nozzle outlets (i.e., holes or slits).[2] This process finds extensive applications in various fields, including microfluidic technology,[3,4] inkjet printing,[5] foods,[6] pharmaceuticals,[7] agriculture,[8] additive manufacturing (i.e., 3D printing)[9] and so on. The breakup process is generally achieved by applying disturbances to the fluid passing through the nozzle, which may involve complex internal geometry,[10] multiphase fluids, and different physics for disturbance introduction, e.g., pressure, ultrasonic, electric fields, etc.

To produce highly controllable droplets, piezoelectric-driven nozzles have received considerable attention and are usually applied in inkjet printing.[11−13] As the core of the piezoelectric driven nozzle, the piezoelectric ceramic realizes the conversion of electrical energy to mechanical energy.[13] By manipulating the applied voltage (including its amplitude, waveform, number of waves, etc.), a pressure pulse can be formed, and then a single drop flows out of the nozzle orifice.[14] Harris et al.[15] produced highly uniform droplets ranging from 0.5 mm to 1.4 mm by creating a stable pulsation. Liou et al.[16] provided the relationship between the driving voltage and the resultant maximum displacement of piezoelectric ceramic (lead zirconate titanate, PZT) membrane. Using the computational fluid dynamics (CFD) simulation and microflow visualization technique, they found that the droplet volume, velocity and configuration are related to the driving waveform. Xiao et al.[17] modeled a directly actuated piezoelectric nozzle by considering piezoelectric effect, solid−liquid interaction and two-phase flow. The systems listed above are drop-on-demand (DOD) systems, in which droplets are ejected from the nozzle one by one. Breakup of liquid jets or sheets is another more efficient way to generate droplets. Vassallo and Ashgriz[18] experimentally explored a nozzle made from an aluminum tube with a piezo-electric to generate disturbances. The influence of frequencies and amplitudes of disturbances on droplet formation has been investigated and four breakup modes have been identified. Wu et al.[19] developed a piezoceramics driven glass nozzle and created a sinusoidal disturbance to break up the liquid jet. They demonstrated that such a nozzle is capable of producing uniform-sized droplets. Although piezoelectric-driven methods have been utilized to create disturbances for liquid jet breakup, the underlying mechanisms remain unknown. In other words, we still do not know how the operational conditions of piezoelectric ceramic can affect the liquid flow in the nozzle and subsequently influence the breakup of the liquid jet ejected from the nozzle.

Theoretical studies on droplet formation through breakup of liquid jets or sheets flowing out of the nozzle have been carried out. Taking jets for an example, Rayleigh[20] conducted theoretical research on breakup of inviscid fluid jet. Their theory indicates that the fluid jet breakup is caused by the

Received: June 15, 2024
Revised: September 4, 2024
Accepted: September 6, 2024
Published: September 17, 2024

https://doi.org/10.1021/acs.iecr.4c02237
Ind. Eng. Chem. Res. 2024, 63, 16915−16927

disturbance from the surrounding medium. With the increase of disturbance level, the liquid jet surface becomes unstable, leading to the breakup. Based on this theory, Weber[21] considered the influence of gas flow dynamics and liquid viscous force on jet breakup, and derived a formula of the optimum disturbance wavelength for jet breakup. Both liquid properties and external forces influence the jet breakup mode. For example, through an experimental investigation, Wang et al.[22] observed that there was a unique hardened breakup mode only when the suspension jet exhibited discontinuous shear thickening behavior. Du and Chaudhuri[23] developed a multiphysics model to study the breakup of charged droplets in an electric field. The droplet breakup from jets may still be subjected to the influence of external forces such as updraft[24] for secondary breakup. These studies improved our fundamental understandings of droplet formation from jet breakup. However, all these efforts focused on characterizing the process outside of the nozzle, the phenomena inside the nozzle remain unknown. Microfluidic system development has become a hot topic in recent years due to the systems' high level of efficiency, repeatability and controllability. By resorting to both experimental and numerical methods, Lu et al.[4] investigated the droplet generation in the microfluidic step emulsification system with a triangular nozzle. They found that compared with a rectangular nozzle, under the dripping regime, a triangular nozzle could produce droplets with better monodispersity. Although their methods may be applicable to the nozzle with different geometries, they cannot deal with external disturbances exerted on the nozzle, e.g., piezoelectric pulsation if available.

In this work, aiming at simulating the complete atomization process, a velocity coupling method was proposed to couple the in-nozzle and out-nozzle models. By resorting to this method, it becomes possible to quantitatively correlate the nozzle operating parameters and droplet formation and further reveal atomization mechanisms. A piezoelectric ceramic nozzle was taken as an example to demonstrate the efficacy of the method.

2. MODELING AND ANALYSIS METHODS

2.1. Geometry Construction. A piezoelectric pulsation-driven glass nozzle was developed by Wu et al.[19,25,26] which can produce monodispersed droplets. Based on the nozzle used in their experimental work, the geometry for this work was constructed (see Figure 1(a)). A 2D axisymmetric model was developed due to the axial symmetric property of the geometry.

The simulation system contains two parts: the part in the nozzle and the part outside of the nozzle. The upper part of this geometry is the nozzle. The liquid (in gray color in Figure 1(a)) flows in a long glass tube (in green color) with an external radius of R_t (m). A piezoelectric ceramic cylinder (with width W_p (m), height H_p (m), red color) is attached to the glass tube. Liquid flows from the nozzle outlet (with radius R_n (m)) into the air domain (white color, with radius R_{on} (m), height H_{on} (m)) to form a liquid jet, which can then be broken into droplets. The terms "part 1" and "part 2" are used to represent the two parts above and below the nozzle outlet, respectively. Several parameters used in the following analyses are also shown in Figure 1, including the droplet diameter in the z direction D_z (m) and the droplet diameter in the r direction D_r (m). Moreover, the length of the unbroken jet is denoted as L_j (m), and the wavelength is denoted as λ (m). The space between two neighboring droplets has a length of S_d (m).

As shown in Figure 1, part 1 is much larger than part 2. The liquid region with gray color has a radius × height of 3.5 mm × 46 mm in part 1, but the radius of part 2 is only 0.45 mm. Note that the radius of the droplet is further smaller than the radius of part 2. Due to the significant size difference between the two parts, it is very difficult to mesh the geometry as a holistic domain. A sufficiently fine mesh in part 2 should be implemented to ensure decent tracking of droplet shape evolution. However, it will lead to an unnecessarily fine mesh in part 1 and hence a high computational cost. Moreover, it is challenging to couple piezoelectricity, fluid-structure interaction, and liquid−gas flow simultaneously in one model. The complicated multiphysics governing equations involved in this work will be described in the next section.

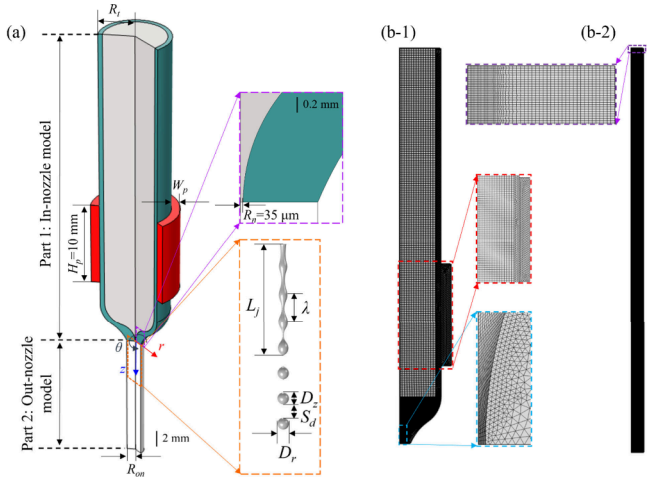

Figure 1. Illustration of the nozzle: (a) geometry (3D view) and (b) mesh constructed for the nozzle. (b-1) and (b-2) are for the in-nozzle model and the out-nozzle model, respectively.

To address the challenges listed above, part 1 and part 2 are modeled separately. Part 1 can then focus on the piezoelectric effect and the fluid-structure interaction, while part 2 can take care of liquid−gas interface tracking. Note that a very small section of the nozzle outlet (with a height of 1/100 of the nozzle radius, i.e., 0.35 μm) should be considered in modeling two-phase flow in part 2. In the following text, the two models are denoted as the "in-nozzle" model and the "out-nozzle" model.

2.2. Governing Equations. In the in-nozzle domain, the piezoelectric ceramic exerts a disturbance on the fluid by periodically deforming the glass, leading to the temporal change of fluid velocity profiles at the nozzle outlet. In the out-nozzle domain, the liquid jet leaving the nozzle breaks into droplets. The following text lists governing equations for the two models.

2.2.1. In-Nozzle Model. 2.2.1.1. Electrostatics. When a voltage is applied to the piezoceramics, an electric field can be generated

$$\nabla \cdot \boldsymbol{D} = 0 \tag{1}$$

$$\boldsymbol{E} = -\nabla U \tag{2}$$

where $\boldsymbol{D}$ (C/m^2) is the electric displacement field; $\boldsymbol{E}$ (V/m) is the electric field; and U (V) is the electric potential.

2.2.1.2. Solid Mechanics. The deformation of glass and piezoelectric ceramics caused by the disturbance of the piezoelectric ceramic will be described by the equation of solid mechanical physics, as shown below,

$$\rho_s \frac{\partial^2 \boldsymbol{X}}{\partial t^2} = \nabla \cdot S \tag{3}$$

https://doi.org/10.1021/acs.iecr.4c02237
Ind. Eng. Chem. Res. 2024, 63, 16915−16927

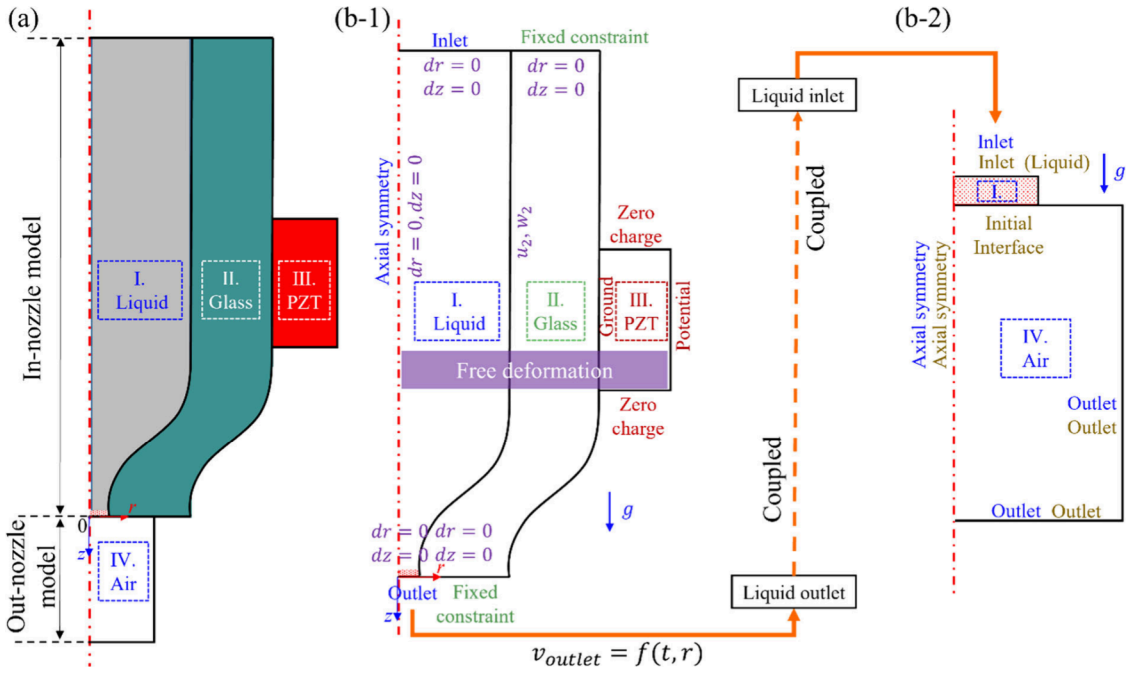

Figure 2. Schematic diagram of (a) the overall atomization process, (b) the initial and boundary conditions of (b-1) the in-nozzle model and (b-2) the out-nozzle model. The in-nozzle model characterizes the piezoelectric pulsation and fluid flow in the atomizer by coupling electrostatics, solid mechanics, fluid-structure interaction, and dynamic mesh methods. The out-nozzle model tracks liquid−gas interface evolution with the level set method.

where ρ_s (kg/m^3) is the mass density, which is the density of glass or piezoelectric ceramic; $\boldsymbol{X}$ (m) is the displacement vector; and S (Pa) is the stress tensor.

For glass, the stress tensor S can be determined using the following equation:

$$S = C_e : \epsilon \tag{4}$$

where $C_e = C(\Gamma,\nu)$, $\epsilon = \frac{1}{2}[(\nabla X)^T + \nabla X]$. C_e is the fourth order elasticity tensor; and ":" represents the double-dot tensor product (i.e., double contraction); Γ (Pa) is Young's modulus; ν is Poisson's ratio; ϵ is the strain, which is a function of displacement.

For piezoelectric ceramics, there is a coupling between stress and the electric field, which is determined by the following constitutive relation:

$$S = c_E : \epsilon - e^T \boldsymbol{E} \tag{5}$$

$$\boldsymbol{D} = e\epsilon + \epsilon_{0,vac}\epsilon_{rS}\boldsymbol{E} \tag{6}$$

where the elasticity matrix c_E (Pa) and coupling matrix e (C/m^2) are based on the material; $\epsilon_{0,vac}$ (F/m) is the permeability of vacuum; and ϵ_{rS} is the relative permittivity based on the material.

The displacement of the glass caused by the voltage applied to the piezoelectric ceramics in this work is the inverse piezoelectric effect. Under the action of an electric field, the solid region is deformed by stress, reflecting the conversion of electrical energy into mechanical energy.

2.2.1.3. Laminar Flow. The flow of fluid in the nozzle is described by laminar flow and is governed by the Navier−Stokes equation. The fluid considered in this work is incompressible. The fluid flow equation is as follows:

$$\rho\nabla\cdot(\boldsymbol{u}) = 0 \tag{7}$$

$$\rho\frac{\partial \boldsymbol{u}}{\partial t} + \rho(\boldsymbol{u}\cdot\nabla)\boldsymbol{u} = \nabla\cdot[-p\boldsymbol{I} + \mu(\nabla\boldsymbol{u} + (\nabla\boldsymbol{u})^T)] + \boldsymbol{F} \tag{8}$$

where ρ is the liquid density, denoted as ρ_L (kg/m^3); μ (Pa·s) is the liquid viscosity; $\boldsymbol{u}$ (m/s) is the velocity vector; p (Pa) is the pressure; $\boldsymbol{I}$ is the unit tensor; and $\boldsymbol{F}$ (N/m^3) is the volume force vector, which is gravity in this work.

2.2.2. Out-Nozzle Model. 2.2.2.1. Level Set for Interface Tracking. In gas−liquid two-phase flow, different phases are represented by the level set function ϕ (ranging from 0 to 1), where 0 and 1 correspond to different pure phases. In this work, $\phi = 0$ represents pure air, and $\phi = 1$ represents pure liquid. The location of the interface between liquid and air is tracked by the contour where $\phi = 0.5$. This interface is determined by solving the following equation:

$$\frac{\partial\phi}{\partial t} + \nabla\cdot(\boldsymbol{u}\phi) = \gamma\nabla\cdot\left(\varepsilon\nabla\phi - \phi(1-\phi)\frac{\nabla\phi}{|\nabla\phi|}\right) \tag{9}$$

where γ (m/s) represents the reinitialization parameter; ε (m) is the interface thickness controlling parameter.

2.2.2.2. Laminar Flow. Liquid flows out from the nozzle, and its velocity continues to follow the principles of laminar flow as described by eqs 7 and 8. The flow in the out-nozzle model is characterized as a two-phase flow with distinct fluid properties. The density ρ (kg/m^3) becomes a function of liquid density, air density, and the level set function, as defined in eq 10. Similarly, the viscosity μ (Pa·s) is defined in eq 11. $\boldsymbol{F}$ includes both gravity and surface tension here. The equation of the surface tension force is provided in eq 12

$$\rho = \rho_G + (\rho_L - \rho_G)\phi \tag{10}$$

$$\mu = \mu_G + (\mu_L - \mu_G)\phi \tag{11}$$

https://doi.org/10.1021/acs.iecr.4c02237
Ind. Eng. Chem. Res. 2024, 63, 16915−16927

$$\boldsymbol{F}_{st} = \nabla\cdot(\sigma(\boldsymbol{I} - (\boldsymbol{nn}^T))\delta) \tag{12}$$

where subscripts G and L represent air and liquid, respectively. The symbol σ corresponds to the surface tension coefficient (N/m); $\boldsymbol{n}$ is the unit normal to the interface; δ is a Dirac delta function positioned at the interface, expressed as

$$\delta = 6|\nabla\phi||\phi(1-\phi)| \tag{13}$$

2.3. Boundary and Initial Conditions. The boundary and initial conditions for both the in-nozzle model and the out-nozzle model are depicted in Figure 2. In Figure 2(b), different colors—blue, green, red, purple, and golden—represent various physics: fluid flow, solid mechanics (including domains II and III), piezoelectric effect, moving mesh and level set, respectively. Specifically, domain I represents the liquid domain, domain II represents the glass, and domain III corresponds to the piezoelectric ceramic. Domain IV includes both air and the liquid. Notably, both the in-nozzle model and the out-nozzle model take into account gravity.

In the in-nozzle model, piezoelectric ceramics apply pulsations on the glass, causing the liquid to flow out of the nozzle outlet with a specific shape. Domain I corresponds to the fluid flow region (see Figure 2(a) and (b-1)). The upper side of domain I is a liquid inlet characterized by a specific flow rate. This inlet operates with a fully developed flow condition, owing to its connection to a lengthy tube at the upper end of the nozzle. In addition, the pressure outlet is specified at the bottom side of domain I.

Domains II and III specify the solid mechanical physical field. Domain II represents the glass and features fixed constraints on its upper and lower boundaries (Figure 2(a)). Domain III is designated as the region for piezoelectric material. In this setup, a piezoelectric ceramic is subject to a sinusoidal potential on the right-hand, characterized by $U = U_{peak}\cdot\sin(2\pi ft)$, while the left side is grounded. Zero charge is applied to both the upper and lower sides of the piezoelectric ceramic, resulting in displacement occurring exclusively in the r direction.

The liquid domain undergoes deformation due to the disturbance applied by the piezoelectric ceramics on the glass. All three domains of I, II, and III are designated for unconstrained deformation. At the junction of domains I and II, the displacement is specified as $\boldsymbol{X}_r$ in the r direction and $\boldsymbol{X}_z$ in the z direction. The axis, upper boundary, and lower boundary of both domain I and domain II are fixed.

For the out-nozzle model (Figure 2(b)), domain I and domain IV are designed for fluid flow and level set physics, respectively. The upper boundary of domain I serves as a liquid inlet, with a velocity profile solution derived from the in-nozzle model. Outlets are positioned on both sides of the air domain. A nonslip boundary condition is imposed on the wall of domain I. The interface between domain I and domain IV marks the initial gas—liquid interface.

2.4. Coupling Method. To utilize the outcomes of the in-nozzle model as the inlet boundary condition for the out-nozzle model, a velocity coupling method is employed. This method aims to derive a velocity formula of the nozzle outlet for seamlessly coupling these two models.

Because the fluid flow at the outlet of the glass tube is in a fully developed laminar state, the velocity profile along the radius at any given time resembles a parabolic shape. Furthermore, the velocity experiences periodic fluctuations over time. Consequently, the associated velocity distribution can be represented as a quadratic function at various moments within a single cycle.

$$v_{t=0} = a_0r^2 + b_0r + c_0 \tag{14}$$

$$v_{t=t_1} = a_1r^2 + b_1r + c_1 \tag{15}$$

$$v_{t=t_2} = a_2r^2 + b_2r + c_2 \tag{16}$$

...

$$v_{t=T} = a_nr^2 + b_nr + c_n \tag{17}$$

Given that the velocity varies over time, the coefficients of the terms within the quadratic function become functions of time as well. Therefore, $a_0, a_1, ..., a_n$ are denoted as $A(t)$; $b_0, b_1, ..., b_n$ are represented as $B(t)$; $c_0, c_1, ..., c_n$ are represented by $C(t)$. The velocity at the nozzle outlet can be formulated as

$$v_{outlet} = A(t)r^2 + B(t)r + C(t) \tag{18}$$

When the electric potential of the piezoelectric ceramics is applied to the glass tube as a sinusoidal function, the velocity within the model exhibits a sinusoidal pattern with periodic variations over time. Therefore, $A(t)$, $B(t)$, and $C(t)$ can be approximated and fitted using sinusoidal functions.

$$A(t) = m_A\cdot\sin(2\pi f(t + \varphi_A/f)) + n_A \tag{19}$$

$$B(t) = m_B\cdot\sin(2\pi f(t + \varphi_B/f)) + n_B \tag{20}$$

$$C(t) = m_C\cdot\sin(2\pi f(t + \varphi_C/f)) + n_C \tag{21}$$

where m_k, φ_k, and n_k (k represents A, B, or C) denote coefficients for amplitude, longitudinal distance, and lateral distance, respectively.

The velocity distribution formula finally becomes

$$\begin{aligned} v_{outlet} = {} & (m_A\cdot\sin(2\pi f(t + \varphi_A/f)) + n_A)r^2 \\ & + (m_B\cdot\sin(2\pi f(t + \varphi_B/f)) + n_B)r \\ & + (m_C\cdot\sin(2\pi f(t + \varphi_C/f)) + n_C) \end{aligned} \tag{22}$$

For each set of parameter conditions, the nozzle outlet will exhibit a unique velocity distribution profile. This profile serves as the velocity boundary condition for the inlet of the out-nozzle model.

2.5. Analysis Methods. To depict the impact of piezoelectric ceramics on the liquid domain within the glass tube, the evolution of the total volume of the liquid domain is characterized as follows:

$$\Delta V_{volume} = V_{volume} - V_{0,volume} \tag{23}$$

where V_{volume} represents the liquid volume, m^3. $V_{0,volume}$ represents the initial volume, m^3.

The mass flow rate of outflow from the nozzle is given by

$$q_{out} = 2\pi\rho_L\int_0^{R_n} v_{outlet}r\ \mathrm{d}r \tag{24}$$

where v_{outlet} represents the velocity at the nozzle outlet, m/s.

To facilitate analysis in this work, a dimensionless time is defined as

$$t^* = t\cdot f \tag{25}$$

For the out-nozzle model, the mass of droplets collected from the bottom of the out-nozzle model is defined as

https://doi.org/10.1021/acs.iecr.4c02237
Ind. Eng. Chem. Res. 2024, 63, 16915−16927

$$m_d = 2\pi\rho_L \int_0^t \int_0^{R_{on}} v_{on}(\varnothing \geq 0.5) r \, dr \, dt \tag{26}$$

where v_{on} (m/s) represents the velocity of the bottom boundary of the out-nozzle model.

The average diameter of the droplet and its aspect ratio are defined to characterize the shape of a droplet,

$$\bar{D} = \frac{D_z + D_r}{2} \tag{27}$$

$$\zeta = \frac{D_z}{D_r} \tag{28}$$

To assess the quality of droplets collected from the nozzle, two parameters are defined:

$$\bar{D}^* = \frac{\bar{D}_{max} - \bar{D}_{min}}{\bar{D}_{min}} \tag{29}$$

which is employed to indicate the size uniformity of droplets. When $\bar{D}^* \leq 1\%$, droplets are considered to demonstrate monodispersity. And,

$$\Delta\zeta = \zeta_{max} - \zeta_{min} \tag{30}$$

which is used to assess the sphericity of droplets. When $\Delta\zeta \leq 0.1$, $0.9 \leq \zeta_{min} \leq 1$, and $1 \leq \zeta_{max} \leq 1.1$, the droplets have achieved a high level of sphericity.

2.6. System Specifications. The parameters and their values for the base case are listed in Table 1. The liquid properties in the base case are adopted from Wu et al.[19] This work examined the flow behavior in the nozzle after implementing 20 cycles of piezo pulsations to ensure that a stabilized flow was reached. The out-nozzle model was built upon the stabilized in-nozzle flow. For the out-nozzle model, droplet collection was started after 10 ms.

Table 1. Parameter Values Used in the Base Case Simulation

Parameters		Notation	Value
Operating and design parameters	Frequency	f	8 kHz
	Peak voltage	U_{peak}	0.5 V
	Inlet flow rate	q_{in}	1.3 g/min
	Nozzle radius	R_n	35 μm
Liquid properties	Density	ρ	989.8 kg/m^3
	Viscosity	μ	54.4 mPa·s
	Surface tension	σ	65.61 mN/m

To ensure the model's accuracy while minimizing the computational expense, both the in-nozzle model and the out-nozzle model in this paper were verified by a mesh independence study. The total number of mesh cells used was 4615 (mesh 1), 6501 (mesh 2), 8839 (mesh 3), 11139 (mesh 4) and 13439 (mesh 5) for the in-nozzle model and 50200 (mesh 1), 72249 (mesh 2), 94195 (mesh 3), 117929 (mesh 4) and 136774 (mesh 5) for the out-nozzle model. The results of displacement and velocity at the nozzle outlet for the in-nozzle model and velocity along the axis for the out-nozzle model were compared. It was found that mesh 4 and mesh 5 offer almost identical results. Taking into account both simulation accuracy and computational time, mesh 4 was adopted for both models in this work (see Figure 1(b)). The mesh elements in the in-nozzle model have a minimum size of 2.3 μm and a maximum size of 175 μm. The in-nozzle model consists of 11139 mesh elements. In order to capture droplet shape evolution, the total number of mesh elements for the out-nozzle model can reach 117929 with a minimum size of 4.375 μm and a maximum size of 7 μm. Detailed mesh independency study can be found in Supporting Information S1. Under this mesh condition, the simulation results show well agreement with experiment results (see Supporting Information S2).

3. RESULTS AND DISCUSSION

3.1. Base Case Analysis. *3.1.1. Results of the In-Nozzle Model.* The piezoelectric ceramic applies a periodic disturbance on the glass tube, causing the tube wall to shift position in the r direction over time. From 0 to $T/4$, the displacement gradually increases, indicating a positive movement of both the piezoelectric ceramic and the glass tube in the r direction (see $t = T/4$ in Figure 3(a)). As time proceeds to $T/2$, the tube wall returns to its initial state (see $t = T/2$ in Figure 3(a)). As time goes further to $3T/4$, a negative displacement emerges, indicating movement in the negative r direction for both the glass tube and the piezoelectric ceramics (see $t = 3T/4$ in Figure 3(a)). Upon reaching T, the displacement gradually reduces to zero, bringing the glass tube back to its initial position (see $t = T$ in Figure 3(a)). Following the characteristic voltage applied by the piezoelectric ceramic, the displacement undergoes periodic changes as outlined above. Moreover, it is evident that the displacement is particularly pronounced in the region adjacent to the piezoelectric ceramics (see Figure 3(a)).

The displacement of both the glass and piezoelectric ceramics leads to a volume change in the liquid domain (Figure 3(b)). Positive displacement leads to an enlargement of the fluid domain's volume beyond its initial value. Negative displacement, however, results in a reduction in the fluid domain's volume. As shown in Figure 3(b), the temporal evolution of this volume deviation (from the initial volume) follows a sinusoidal function,

$$\Delta V_{volume} = A_v \sin(2\pi f t) \tag{31}$$

The periodic change in the volume of the liquid domain directly influences the flow field within that domain. Changing the nozzle volume leads to a temporal evolution of velocity within a cycle, characterized by an initial increase followed by a subsequent decrease (as observed in the magnified view in Figure 3(a)). Similarly, the periodic variation in the fluid domain volume causes fluctuations in the flow rate at the nozzle outlet, as illustrated in Figure 3(c). During the phase of volume increase ($0-T/4$), the outflow rate gradually ascends from its minimum value to the initial inflow rate. As the fluid domain volume returns to its initial state ($T/4-T/2$), the flow continues to rise. Subsequently, as the liquid domain volume progressively contracts toward its minimum ($T/2-3T/4$), the flow rate decreases back to the initial rate. When the volume increases back to the initial position ($3T/4-T$), the flow continues to decrease, reaching its minimum outflow rate. These changes happen periodically.

The relationship between the change in the outflow rate and the volume evolution might appear counterintuitive. This unexpected phenomenon can be rationalized by delving into the intricate connection between volume change and outlet flow rate. The relationship can be expressed as

$$q_{out} = q_{in} - \rho_L \frac{dV}{dt} \tag{32}$$

Substituting eqs 23 and 31 into eq 32

$$q_{out} = q_{in} - 2\pi f \rho_L A_v \cos(2\pi f t) \tag{33}$$

https://doi.org/10.1021/acs.iecr.4c02237
Ind. Eng. Chem. Res. 2024, 63, 16915−16927

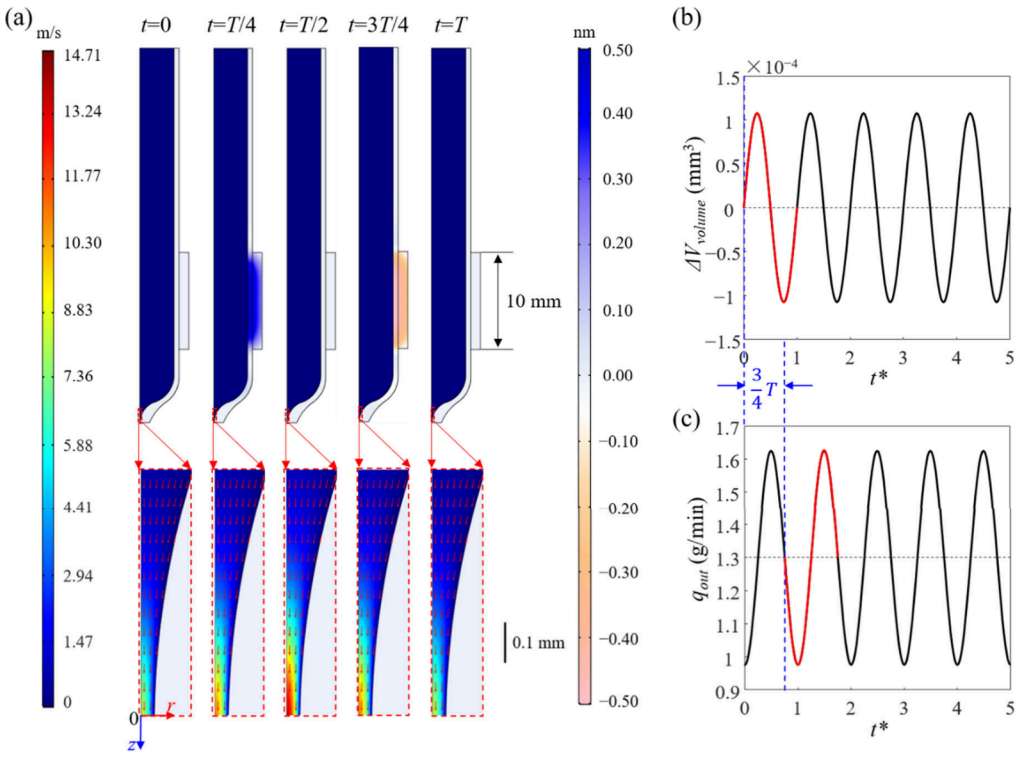

Figure 3. Results of the in-nozzle model for the base case: (a) evolution of the nozzle wall displacement and fluid velocity distribution in a single cycle. The left color bar indicates the magnitude of the fluid velocity, while the right color bar gives the displacement of the piezoceramic component, (b) the evolution of ΔV_{volume} over time, and (c) the evolution of q_{out} over time.

Equations 31 and 33 show that the evolutions of the volume and outflow rate exhibit a phase lag of $3T/4$.

3.1.2. Coupling of Models. The arrows in the enlarged figure in Figure 3(a) indicate that the liquid's motion consistently aligns with the positive z direction, which corresponds to the initial direction of the fluid flow. The velocity along the r direction can be neglected. Hence, the velocity in the z direction of the in-nozzle model is selected as the inlet boundary condition for the out-nozzle model. Taking the first cycle as an example, the velocity distribution along the z direction during this cycle is shown in Figure 4. The velocity in the z direction gradually increases (see 0 to $T/2$ in Figure 4(a)) and subsequently decreases over time (see $T/2$ to T in Figure 4(a)), which aligns with the temporal changes in flow rate (Figure 3(c)). The velocity distribution at the nozzle outlet exhibits a parabolic shape, indicating a fully developed laminar flow state.

The velocity mapping method was employed to derive the velocity at the nozzle outlet. Using the velocity data from the first cycle as an example, the velocity distribution along the nozzle outlet conforms to the quadratic function form (as defined in Eq's. (14−17)). A series of time-dependent coefficients a_0, a_1, ..., a_n, b_0, b_1, ..., b_n, c_0, c_1, ..., b_n, i.e., A, B, and C, can be obtained. These data are illustrated in Figure 4 (b-d) using black asterisks. For fitting, eqs 19−21) are adopted to fit those data, which yields A, B, and C as a function of time. $A(t) = 2.2029 \times 10^9 \times sin(2\pi f(t - 0.245/f)) + 8.9525 \times 10^9$, $B(t) = 5.5064 \times 10^3 \times sin(2\pi f(t - 0.45/f)) - 6.7036 \times 10^3$, $C(t) = 2.8113 \times sin(2\pi f(t + 0.245/f) - 11.0166)$. The fitting curve matches the simulated values very well, indicating an accurate representation of the relationship.

Therefore, the velocity formula for the nozzle outlet in the base case becomes

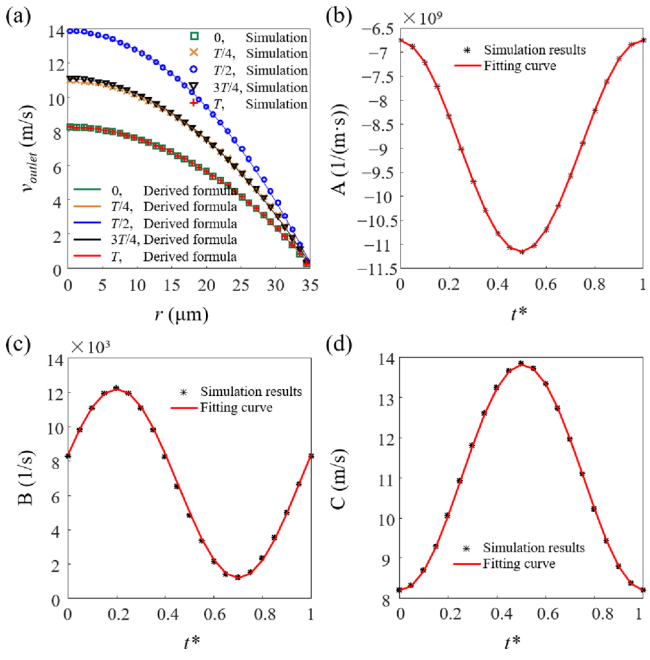

Figure 4. Coupling of in-nozzle and out-nozzle models: (a) the distribution of z-direction velocity along the nozzle outlet, (b-d) the variations of A, B, and C with respect to time, along with their corresponding fitting curves within a single cycle.

https://doi.org/10.1021/acs.iecr.4c02237
Ind. Eng. Chem. Res. 2024, 63, 16915−16927

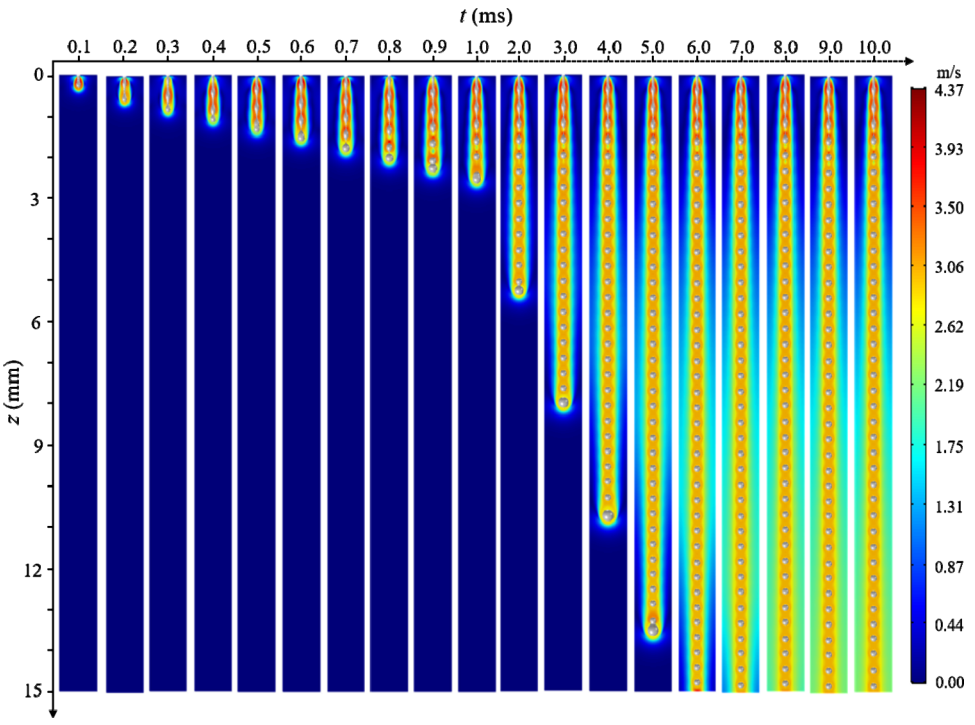

Figure 5. Liquid jet formation and breakup in 10 ms. 3D gas−liquid interfaces were plotted in metallic gray color to help readers identify the shape of droplets. The color bar corresponds to the gas velocity. A new figure showing 2D interfaces has been added in the Supporting Information S3, so that readers can see velocities of both phases.

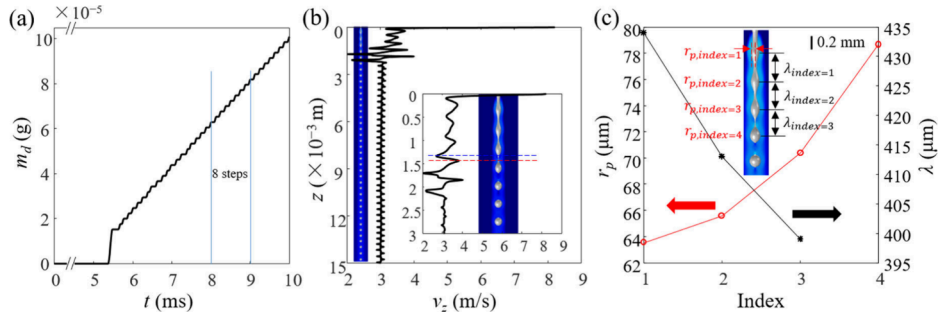

Figure 6. Analysis of droplets: (a) the total weight of droplets collected at the outlet as a function of time, (b) the velocity distribution along the axis and the shape of the liquid jet at 10 ms. The small inset provides an enlarged view of a specific region, and the blue and red dashed lines indicate the locations of the minimum and maximum velocities, respectively, for a thin liquid filament connecting two neighboring droplets that are about to separate, and (c) the perturbations' amplitude and wavelength of the liquid jet at 10 ms. The "Index" represents the sequence number for the perturbation and wave shown in the inset. The inset figure has a size of 2.20 × 0.38 mm^2.

$$
\begin{aligned}
v_{outlet} &= (m_A \cdot \sin(2\pi f(t + \varphi_A/f)) + n_A)r^2 \\
&\quad + (m_B \cdot \sin(2\pi f(t + \varphi_B/f)) + n_B)r \\
&\quad + (m_C \cdot \sin(2\pi f(t + \varphi_C/f)) + n_C) \\
&= (2.2029 \times 10^9 \times \sin(2\pi f(t - 0.245/f)) \\
&\quad + 8.9525 \times 10^9)r^2 + (5.5064 \times 10^3 \\
&\quad \times \sin(2\pi f(t - 0.45/f)) - 6.7036 \times 10^3)r \\
&\quad + (2.8113 \times \sin(2\pi f(t + 0.245/f) - 11.0166))
\end{aligned} \tag{34}
$$

The derived velocity formula for the nozzle outlet is compared with the simulated values, and the comparison offers perfect agreement (see Figure 4(a)). As a result, the aforementioned formula (eq 34) is used to serve as the inlet velocity boundary condition for the out-nozzle model in the base case.

3.1.3. Results of the Out-Nozzle Model. This part of the simulation focuses on the intricate process of liquid jet formation followed by its fragmentation into droplets. At t = 0.1 ms (see Figure 5), a liquid jet emerges near the nozzle, and as time proceeds, the liquid jet extends progressively. The jet does not adopt a regular cylindrical shape with a constant diameter. Instead, it exhibits substantial waviness and thickness variations. This behavior can be attributed to the influence of the disturbance applied by the piezoelectric ceramic. As time reaches 0.8 ms, the lower end of the fluctuating liquid jet starts to break up. Subsequently, the droplets detach sequentially from this point, giving rise to a sequence of individual droplets. Under the periodic perturbation imposed by the piezoelectric ceramic, the droplets demonstrate a nearly uniform distribution.

The mass of droplets collected at the outlet over 10 ms is recorded. As shown in Figure 6(a), m_d remains at 0 until approximately 5.4 ms, when the first droplet starts to exit the

https://doi.org/10.1021/acs.iecr.4c02237
Ind. Eng. Chem. Res. 2024, 63, 16915−16927

outlet. Subsequently, successive droplets continue to exit. Figure 6(a) shows a series of regular steps, which indicate that these droplets possess nearly identical masses. Furthermore, taking 8−9 ms as an example, 8 steps are observed (8 droplets in 1 ms, i.e., 8000 droplets in one second), which precisely matches the applied frequency of 8 kHz. This observation implies the substantial influence of frequency on the positions at which jet breakup takes place. Additionally, the mean droplet size can be estimated as $\frac{4\pi}{3}\left(\frac{\hat{D}}{2}\right)^3\rho_L = \frac{q_{in}}{f}$, i.e.,

$$\hat{D} = \left(\frac{6q_{in}}{\pi\rho_L f}\right)^{1/3} \tag{35}$$

Mu et al.[27] also adopted the same approach to indicate the relationship between droplet size and disturbance frequency ($f = Q_1/\left(\frac{1}{6}\pi D^3\right)$).

Figure 6(b) shows the velocity distribution along the axis at 10 ms. A snapshot of the jet at 10 ms is also given. Notably, the liquid jet experiences a drastic velocity drop from approximately 8 m/s to 3−4 m/s once leaving the small nozzle outlet. This behavior can be attributed to mass conservation. This high velocity suggests that the movement of the liquid jet is primarily governed by the inertial force during the initial stage.[28] In the subsequent ∼2 mm away from the nozzle, the liquid jet experiences breakup, with the velocity curve displaying obvious perturbations. In the range of distance beyond 2 mm from the nozzle, uniformly distributed droplets can be observed, and the associated velocity distribution demonstrates regular oscillations.

By examining the correlation between the shape of the liquid jet and the velocity distribution at distances ranging from 0 mm to 3 mm (see the inset in Figure 6(b)), it becomes apparent that the positions of the maximum and minimum velocities (illustrated by dashed lines) are located at both ends of the liquid filament that connects two neighboring droplets. This discrepancy in velocity is caused by the surface tension, which drives the jet to undergo fragmentation and break into spherical droplets. According to Rayleigh theory[20] and Weber theory,[21] the disturbance propagates downward and grows in amplitude, which causes the amplitude of the liquid jet perturbation to gradually expand and the wavelength to decrease. This trend has been demonstrated by the curves in Figure 6(c), reflecting the influence of surface tension and its role in driving the process of droplet breakup.

In addition to surface tension, the process of droplet formation is influenced by other forces, such as viscous force, inertial force, and gravity. Some dimensionless numbers are used to assess the significance of these forces. The Bond number $Bo = \rho g L^2/\sigma$ characterizes the relative importance of gravity and surface tension. The Weber number $We = \rho u^2 l/\sigma$ indicates the relative importance of the inertial effect and surface tension. The Reynolds number $Re = lu\rho/\mu$ demonstrates the relative importance of the inertial effect and viscous effect. In this work, the small value of Bo (i.e., $1.15 \times 10^{-3} \ll 1$) indicates that surface tension plays a dominant role over gravity. The high velocity of the liquid jet exiting the nozzle results in a high We value of 101.70, indicating that the inertial effect is more significant than the surface tension at this stage. Subsequently, the We number decreases to ∼20 when the jet breaks into droplets. This justifies that the increasing influence from surface tension contributes to jet breakup. The Reynolds number is close to 10 (specifically, 14.94 when the liquid jet exits the nozzle and 9.66 after jet breakup), which indicates that the inertial effect is more pronounced than the viscous effect. It can be concluded that surface tension and inertial forces are two dominant forces in controlling droplet formation in this work.

The size distribution of collected droplets is a critical indicator for powder quality evaluation. In this work, 50 droplets were collected from the bottom of the out-nozzle model, starting from 10 ms, and their sizes were quantified. The distributions of the average diameter and the aspect ratio of collected droplets for the base case are depicted in Figure 7. For the average diameter

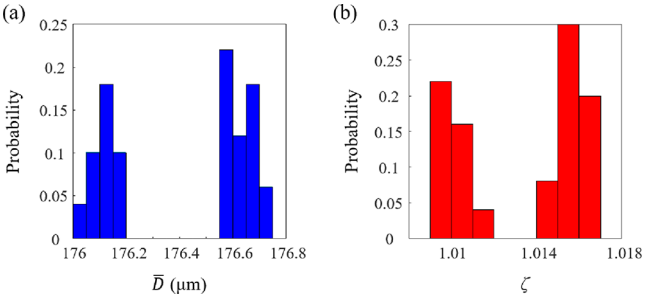

Figure 7. Distributions of (a) average diameter and (b) aspect ratio of droplets in the base case.

distribution (Figure 7(a)), a bin width of 0.05 μm is used, and the size ranges from 176 to 176.8 μm. According to eq 29, $\bar{D}^*$ becomes 0.4%, which is less than 1%. Monodispersed droplets are thus generated in this case.

The average diameter of the droplets is 176.42 μm, which is 2.52 times the diameter of the nozzle (70 μm). A bin width of 0.001 is employed to show the distribution of the aspect ratio. As shown in Figure 7(b), the difference between the maximum and minimum ratios is not even greater than 0.01. According to the criterion of $\Delta\zeta \le 0.1 \cap 0.9 \le \zeta_{min} \le 1 \cap 1 \le \zeta_{max} \le 1.1$, atomized droplets in this case achieve satisfactory sphericity.

3.2. Effects of Different Frequencies of Pulsation. This section explores the impact of different frequencies of piezoelectric pulsation on the liquid jet flow and the distribution of atomized droplets. The evolutions of the volume deviation of the nozzle and the flow rate at the nozzle outlet are presented in Figure 8(a) and (b), respectively. The time duration from 1 to 1.3 ms covers different numbers of cycles for cases with frequencies ranging from 2 kHz to 16 kHz.

Using the dimensionless time (eq 25) as the r-axis to replot the dynamic curves yields two clean subplots in Figure 8(c) and (d). It is interesting to note that the maximum volume deviation of the nozzle does not change with the frequency (Figure 8(c)), while the maximum flow rate at the nozzle outlet increases with the frequency (Figure 8(d)). This phenomenon can be explained by Eq's. (31) and (33), which show that the peak volume deviation is frequency-independent, while the deviation of outlet flow rate from the constant inlet flow rate (i.e., $\Delta q = q_{out} - q_{in}$) is a linear function of frequency.

Figure 9 illustrates the droplet distribution at 10 ms under various frequencies. When the frequency is set as 1 kHz or 2 kHz, satellite droplets can be observed in the vicinity of the primary droplets. The formation of satellite droplets is due to the large spacing between primary liquid droplets at low frequencies when the oscillation of the nozzle outlet flow rate is relatively insignificant (Figure 8(d)). When the thin liquid thread connecting two neighboring droplets breaks, it cannot merge

https://doi.org/10.1021/acs.iecr.4c02237
Ind. Eng. Chem. Res. 2024, 63, 16915−16927

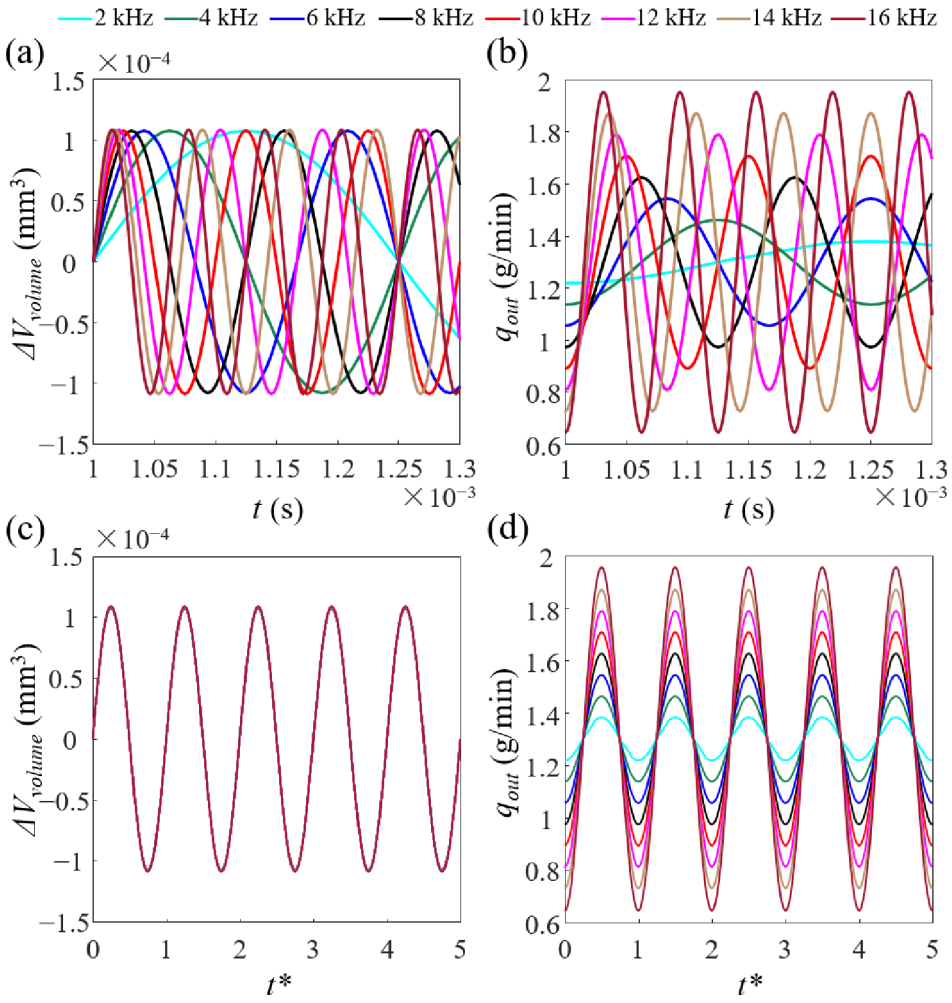

Figure 8. Evolution of volume deviation and flow rate at the nozzle outlet under different frequencies: (a) and (c) are volume deviation over real-time and dimensionless time, respectively, (b) and (d) are flow rate over real-time and dimensionless time, respectively.

with the primary droplet because of the considerable distance between them, leading to the formation of smaller satellite droplets. With an increase in frequency (from 3 kHz to 10 kHz), the distance between neighboring droplets decreases accordingly, leading to a smaller droplet size as well. This trend agrees with the estimation of droplet size by eq 35. As the frequency continues to increase (>10 kHz), although the deviation of outlet flow is more significant (Figure 8(d)), the gap between droplets further decreases, eventually resulting in merged droplets. It is also observed that the length of the liquid jet initially decreases and then increases with increasing frequency. The above analysis can be used to understand this trend.

To quantitatively investigate the droplet size distribution under different frequencies, 50 droplets were collected from the bottom of the out-nozzle model starting from 10 ms, and their sizes were analyzed. The results of two representative frequencies are presented in Figure 10 (complete distributions under all frequencies are shown in Figure S3.1), depicting the distributions of the average diameter and aspect ratio of droplets under different frequencies. In Figure 10, the bin width for the average diameter is set to 10 μm. At a frequency of 1 kHz, the droplet size spans from 0 to 450 μm. According to eq 29, $\overline{D}^* \gg$ 100% and reaches 4822.49%. This indicates a widely dispersed size distribution. With an increase in frequency to 2 kHz and 3 kHz, the size distributions become narrower. $\overline{D}^*$ is reduced to 1023.73% and 1815.18%, respectively, still far more than 100%. As the frequency further increases within the range of 4 kHz ~ 9 kHz, the droplet size distribution remains uniform with size differences of less than 10 μm. $\overline{D}^*$ is less than 1% for all cases from 4 kHz to 9 kHz (i.e., 0.34%, 0.35%, 0.37%, 0.40%, 0.40%, and 0.42%, respectively), which indicates a monodisperse distribution (see subplots with a star in Figure 10 (and Figure S3.1). As the frequency continues to rise beyond 9 kHz, the droplets gradually lose their monodispersity. For cases from 10 kHz to 16 kHz, $\overline{D}^*$ is 88.60%, 46.08%, 50.77%, 111.69%, 59.17%, 127.06% and 6583.36%, respectively. Especially for the case of 16 kHz, the droplet size covers a wide range from 0 to 368.26 μm, with each size bin occupying no more than 10%.

With a bin width of 0.1, it can be observed that when the frequency is below 4 kHz, $\Delta\zeta$ is larger than 0.1 (i.e., 1.61, 0.70, and 1.29, respectively, according to eq 30), implying that some droplets exhibit elongated or flattened shapes. As the frequency increases within the range of 4 kHz ~ 9 kHz (see subplots with a star in Figure 10), the aspect ratios stabilize within the range of 1 $\pm$ 0.1. $\Delta\zeta$ is 0.0084, 0.0072, 0.0072, 0.0073, 0.0073, 0.0074 and 0.0090, respectively, satisfying $\Delta\zeta \leq 0.1$. For these cases, droplets maintain a spherical shape. Beyond this frequency range, as the frequency continues to increase, the aspect ratios become widely dispersed again.

https://doi.org/10.1021/acs.iecr.4c02237
Ind. Eng. Chem. Res. 2024, 63, 16915−16927

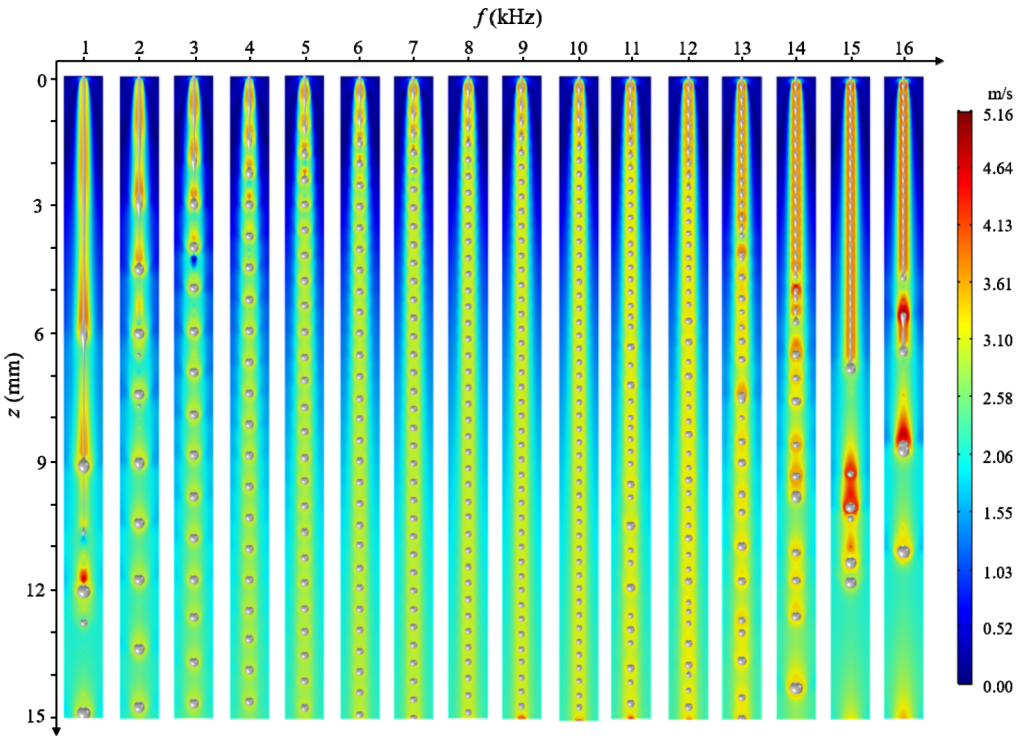

Figure 9. Droplet distribution under different frequencies at 10 ms. 3D gas−liquid interfaces were plotted in metallic gray color to help readers identify the shape of droplets. The color bar corresponds to the gas velocity. A new figure showing 2D interfaces has been added in the Supporting Information S3, so that readers can see velocities of both phases.

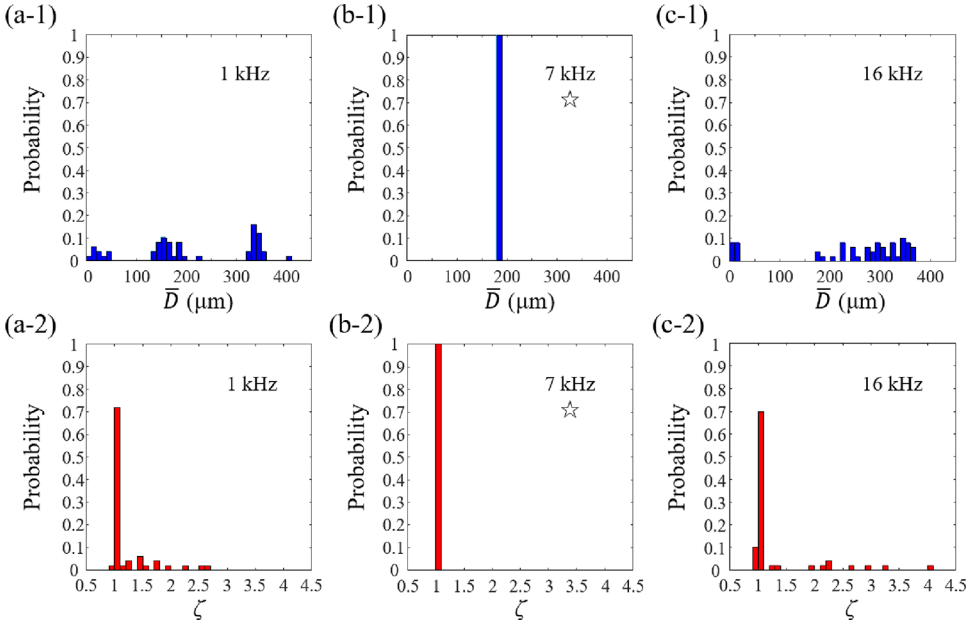

Figure 10. Distributions of the average diameter (displayed in blue) and aspect ratio (shown in red) of droplets atomized under 1 kHz, 7 kHz and 16 kHz. Results under other frequencies are listed in the Supporting Information S4. The star symbol "☆" is used to indicate the cases that can offer decent monodispersity and sphericity.

The probability distribution of the average diameter and aspect ratio under different frequencies (see Figure S3.1) follows the same trend. Droplets in the range of 4 kHz to 9 kHz exhibit a monodisperse distribution and maintain a spherical shape. Frequencies that are either too small or too large result in a more dispersed distribution.

Further quantitative characterization of atomized droplets can be found in Figure 11. The red circles in Figure 11(a) represent the droplet diameter estimated based on eq 35, indicating a decreasing trend with increasing frequency. The simulation results for cases of 4 kHz to 9 kHz match the theoretical estimation well (see comparison in Figure 11(a)) and consistent with that observed in published papers.[19,27] Under other frequencies, however, deviations between estimated and simulated results can be observed. Equation 35 should be a reliable model to estimate the size of monodispersed droplets.

https://doi.org/10.1021/acs.iecr.4c02237
Ind. Eng. Chem. Res. 2024, 63, 16915−16927

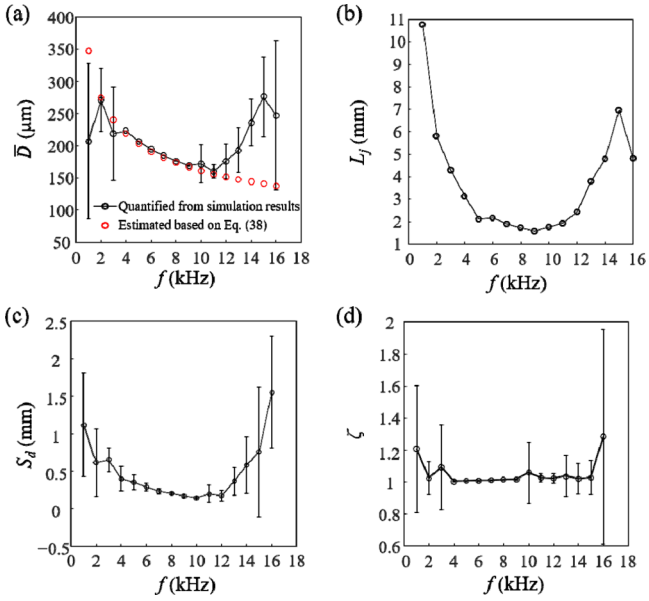

Figure 11. Droplet distributions under different frequencies: (a) comparison of simulation results and estimated results of average diameter, (b) length of the liquid jet at 10 ms, (c) spacing between two neighboring droplets at 10 ms, and (d) aspect ratio of droplets. (a) and (d) are analyzed based on 50 droplets collected starting from 10 ms.

Taking into account the presence of small satellite droplets and the coalescence of droplets, the average droplet size varies between 2.29 and 3.94 times the nozzle size. As discussed before, with increasing frequency, the liquid jet first decreases and then increases (Figure 11(b)). The spacing between two neighboring droplets demonstrates the same trend (Figure 11(c)). The presence of extremely small, nonspherical droplets contributes to the increased aspect ratio at the lowest and highest frequencies (Figure 11(d)).

4. CONCLUSIONS

In this work, a new modeling approach is introduced to numerically investigate the droplet formation process through atomization. The unique feature of this approach is to couple two individually simulated models (i.e., in-nozzle and out-nozzle models) through velocity coupling. This method is especially useful for atomization systems involving multiple complex physics, a large number of droplets with a wide range of size distributions, and intricate nozzle geometry.[21] By resorting to this method, one should be able to systematically carry out in silico investigations on how the operation of the nozzle can influence jet formation and succeeding droplet formation through jet breakup.

Numerical investigation of droplet formation through a piezoceramic glass nozzle was used to demonstrate the power of the developed modeling method. For this specific nozzle, sinusoidal pulsations are applied by the piezoelectric ceramics to the glass tube. This cyclic pulsation results in periodic fluctuations of the volume of the liquid domain in the nozzle, subsequently influencing both the flow rate and the liquid velocity at the nozzle outlet. In a base case, the liquid discharged from the nozzle experiences pulsations induced by the piezoelectric ceramic, resulting in the formation of a wavy fluid jet. The wavelength of the jet progressively shortens, eventually leading to its breakup into droplets. The resulting droplets assume a spherical shape due to the dominance of surface tension and descend with a stable velocity. Furthermore, the impact of different frequencies applied to the piezoceramic on droplet formation was explored, which was selected as a representative parametric study to demonstrate the model's effectiveness. Although varying the frequency does not influence the displacement and volume deviation of the nozzle, it notably affects the outlet flow rate. Based on the proposed model, the results show that at lower frequencies (<4 kHz), the piezoelectric ceramic induces less pronounced disturbances, resulting in larger gaps between droplets, often leading to the coexistence of main droplets and satellite droplets. As the frequency increases (4−9 kHz), both droplet size and spacing decrease, leading to the formation of uniformly sized droplets. As the frequency continues to increase (>9 kHz), the distance between droplets becomes even closer, eventually leading to their coalescence. Parametric studies of other key operating conditions, such as voltage, inflow rate, and nozzle radius, will be carried out in our future study.

■ ASSOCIATED CONTENT

Supporting Information

The Supporting Information is available free of charge at https://pubs.acs.org/doi/10.1021/acs.iecr.4c02237.

Mesh independence study, experimental validations and additional simulation results (PDF)

■ AUTHOR INFORMATION

Corresponding Author

Jie Xiao − *Particle Engineering Laboratory (China Petroleum and Chemical Industry Federation), School of Chemical and Environmental Engineering, College of Chemistry, Chemical Engineering and Materials Science, Soochow University, Suzhou 215123, China;* orcid.org/0000-0001-7842-7862; Email: jie.xiao@suda.edu.cn

Authors

Jinping Zha − *Particle Engineering Laboratory (China Petroleum and Chemical Industry Federation), School of Chemical and Environmental Engineering, College of Chemistry, Chemical Engineering and Materials Science, Soochow University, Suzhou 215123, China*

Liangchao Shang − *Particle Engineering Laboratory (China Petroleum and Chemical Industry Federation), School of Chemical and Environmental Engineering, College of Chemistry, Chemical Engineering and Materials Science, Soochow University, Suzhou 215123, China*

Winston Duo Wu − *Particle Engineering Laboratory (China Petroleum and Chemical Industry Federation), School of Chemical and Environmental Engineering, College of Chemistry, Chemical Engineering and Materials Science, Soochow University, Suzhou 215123, China*

Xiao Dong Chen − *Particle Engineering Laboratory (China Petroleum and Chemical Industry Federation), School of Chemical and Environmental Engineering, College of Chemistry, Chemical Engineering and Materials Science, Soochow University, Suzhou 215123, China*

Complete contact information is available at: https://pubs.acs.org/10.1021/acs.iecr.4c02237

Notes

The authors declare no competing financial interest.

■ ACKNOWLEDGMENTS

We are grateful for the financial support from the National Natural Science Foundation of China (21978184, 22278284), the "Jiangsu Innovation and Entrepreneurship (Shuang Chuang) Program", the "Jiangsu Specially Appointed Professors Program", and the "Priority Academic Program Development (PAPD) of Jiangsu Higher Education Institutions".

■ NOMENCLATURE

Symbols

A	i.e., a_0, a_1, ..., a_n, functions of coefficients of quadratic term at different times (1/(m·s))
A_v	Amplitude of the volume change (m^3)
B	i.e., b_0, b_1, ..., b_n, functions of coefficients of primary term at different times (1/s)
C	i.e., c_0, c_1, ..., c_n, functions of coefficients of constant term at different times (m/s)
C_e	4th order elasticity tensor (−)
c_E	Elasticity matrix (Pa)
$\boldsymbol{D}$	Electric displacement field (C/m^2)
D_r	Droplet diameter in the r direction (m)
D_z	Droplet diameter in the z direction (m)
$\overline{D}$	Average diameter of droplet (m)
$\hat{D}$	Estimated mean droplet size (m)
$\overline{D}^*$	Dispersity of droplets (−)
$\boldsymbol{E}$	Electric field (V/m)
e	Coupling matrix (C/m^2)
$\boldsymbol{F}$	Volume force vector (N/m^3)
f	Frequency (kHz)
H_p	Height of piezoelectric ceramic (m)
H_{on}	Height of the air domain in out-nozzle model (m)
$\boldsymbol{I}$	Unit tensor (−)
L_j	Length of the unbroken jet (m)
m_d	Mass of droplets (g)
m, φ, n	Coefficients for amplitude, longitudinal distance, and lateral distance
$\boldsymbol{n}$	Unit normal to the interface (−)
p	Pressure (Pa)
q_{in}	Inflow rate (g/min)
q_{out}	Outflow rate from the nozzle (g/min)
R_n	Radius of the outlet of in-nozzle model (m)
R_{on}	Radius of the air domain in out-nozzle model (m)
R_t	External diameter of glass tube (m)
r, z, θ	Cylindrical coordinates (m, m, °)
r_p	Radius of perturbations of the liquid jet (m)
$\boldsymbol{S}$	Stress tensor (Pa)
S_d	Length of the space between neighboring droplets (m)
T	Cycle (s)
t	Time (s)
t^*	Dimensionless time (−)
U	Electric potential (V)
$\boldsymbol{u}$	Velocity vector (m/s)
V_{volume}	Liquid volume (m^3)
$V_{0,volume}$	Initial volume (m^3)
v	Velocity (m/s)
v_{outlet}	Velocity at the nozzle outlet (m/s)
v_{on}	Velocity of the bottom boundary of the out-nozzle model (m/s)
W_p	Width of piezoelectric ceramic (m)
$\boldsymbol{X}$	Displacement vector (m)

Greek Letters

Γ	Young's modulus (Pa)
γ	Reinitializetion parameter (m/s)
Δ	Difference value (−)
δ	Dirac delta function positioned at interface (−)
ε	Interface thickness controlling parameter (m)
ϵ	Strain (−)
$\epsilon_{0,vac}$	Permeability of vacuum (F/m)
ϵ_{rS}	Relative permittivity (−)
ζ	Aspect ratio of the droplet (−)
λ	Wavelength of the unbroken jet (m)
μ	Liquid viscosity (mPa·s)
ν	Poisson's ratio (−)
ρ	Density (kg/m^3)
ρ_L	Liquid density (kg/m^3)
ρ_s	Mass density (kg/m^3)
σ	Surface tension coefficient (N/m)
ϕ	Level set function (−)

Superscript

T	Matrix transposition

Subscripts

G	Gas (air in this work)
k	A, B, or C in A(t), B(t) or C(t)
L	Liquid
max	Maximum value
min	Minimum value
$peak$	Peak value
st	Surface tension

■ REFERENCES

(1) Kooij, S.; Sijs, R.; Denn, M. M.; Villermaux, E.; Bonn, D. What determines the drop size in sprays? *Phys. Rev. X* **2018**, *8* (3), 031019.
(2) Lin, S. P. Introduction. In *Breakup of Liquid Sheets and Jets*; Cambridge University Press: Cambridge, 2003; pp 1−6.
(3) Sontti, S. G.; Atta, A. Numerical insights on controlled droplet formation in a microfluidic flow-focusing device. *Ind. Eng. Chem. Res.* **2020**, *59* (9), 3702−3716.
(4) Lu, Y.; Liu, X.; Liu, X.; Chen, Y. Robust generation of monodisperse droplets using a microfluidic step emulsification device with triangular nozzle. *AIChE J.* **2023**, *69*, No. e18202.
(5) Zhang, Y.; Li, D.; Liu, Y.; Wittstock, G. Inkjet printing in liquid environments. *Small* **2018**, *14* (27), 1801212.
(6) Wang, N.; Fu, N.; Chen, X. D. The extent and mechanism of the effect of protectant material in the production of active lactic acid bacteria powder using spray drying: A review. *Curr. Opin. Food Sci.* **2022**, *44*, 100807.
(7) Baumann, J. M.; Adam, M. S.; Wood, J. D. Engineering advances in spray drying for pharmaceuticals. *Annu. Rev. Chem. Biomol.* **2021**, *12*, 217−240.
(8) Doruchowski, G.; Holownicki, R. Environmentally friendly spray techniques for tree crops. *Crop Prot.* **2000**, *19* (8−10), 617−622.
(9) Soong, S. Z.; Lai, W. L.; Kay Lup, A. N. Atomization of metal and alloy powders: Processes, parameters, and properties. *AIChE J.* **2023**, *69*, No. e18217.
(10) Jin, W.; Xiao, J.; Ren, H.; Li, C.; Zheng, Q.; Tong, Z. Three-dimensional simulation of impinging jet atomization of soft mist inhalers using the hybrid VOF-DPM model. *Powder Technol.* **2022**, *407*, 117622.
(11) Wei, H.; Xiao, X.; Yin, Z.; Yi, M.; Zou, H. A waveform design method for high DPI piezoelectric inkjet print-head based on numerical simulation. *Microsyst. Technol.* **2017**, *23* (12), 5365−5373.
(12) Dou, J.; Wang, X.; Li, K.; Wang, S.; Yan, S.; Zhou, J.; Zou, H. Study on the dynamic characteristics of piezoelectric inkjet print head with basic excitation methods. *Microsyst. Technol.* **2019**, *25* (8), 2985−2992.
(13) Li, K.; Liu, J.-k.; Chen, W.-s.; Zhang, L. Controllable printing droplets on demand by piezoelectric inkjet: applications and methods. *Microsyst. Technol.* **2018**, *24* (2), 879−889.

https://doi.org/10.1021/acs.iecr.4c02237
Ind. Eng. Chem. Res. 2024, 63, 16915−16927

(14) Dong, H.; Carr, W. W.; Morris, J. F. An experimental study of drop-on-demand drop formation. *Phys. Fluids* **2006**, *18* (7), 072102.
(15) Harris, D. M.; Liu, T.; Bush, J. W. M. A low-cost, precise piezoelectric droplet-on-demand generator. *Exp. Fluids* **2015**, *56* (4), 1−7.
(16) Liou, T. M.; Chan, C. Y.; Shih, K. C. Effects of actuating waveform, ink property, and nozzle size on piezoelectrically driven inkjet droplets. *Microfluid. Nanofluid.* **2010**, *8* (5), 575−586.
(17) Yuan, X.; Wei, Z.; Pan, W.; Hongying, L. Numerical simulation and experimental research of micro-droplet generation by directly actuated piezoelectric nozzle. *J. Mech. Eng.* **2020**, *56* (17), 233−239.
(18) Vassallo, P.; Ashgriz, N. Satellite formation and merging in liquid jet breakup. *Proc. R. Soc. London, Ser. A* **1991**, *433* (1888), 269−286.
(19) Wu, W. D.; Lin, S. X.; Chen, X. D. Monodisperse droplet formation through a continuous jet break-up using glass nozzles operated with piezoelectric pulsation. *AIChE J.* **2011**, *57* (6), 1386−1392.
(20) Rayleigh, L. On the instability of jets. *P. London Math. Soc.* **1878**, *s1-10*, 4−13.
(21) Weber, C. The break-up of liquid jets. *Z. Angew. Math. Mech.* **1931**, *11*, 136−154.
(22) Wang, Z. Y.; Zhao, H.; Li, W. F.; Xu, J. L.; Liu, H. F. Primary breakup of shear-thickening suspension jet by an annular air jet. *AIChE J.* **2022**, *68* (4), No. e17579.
(23) Du, W.; Chaudhuri, S. A multiphysics model for charged liquid droplet breakup in electric fields. *Int. J. Multiphase Flow* **2017**, *90*, 46−56.
(24) Liu, H. F.; Wang, Y. F.; Zhao, H.; Li, W. F.; Xu, J. L. Drop breakup and entrainment in the updraft. *AIChE J.* **2022**, *68* (8), No. e17704.
(25) Wu, W. D.; Amelia, R.; Hao, N.; Selomulya, C.; Zhao, D.; Chiu, Y.-L.; Chen, X. D. Assembly of uniform photoluminescent micro-composites using a novel Micro-Fluidic-Jet-Spray-Dryer. *AIChE J.* **2011**, *57* (10), 2726−2737.
(26) Wu, W. D.; Liu, W.; Gengenbach, T.; Woo, M. W.; Selomulya, C.; Chen, X. D.; Weeks, M. Towards spray drying of high solids dairy liquid: Effects of feed solid content on particle structure and functionality. *J. Food Eng.* **2014**, *123*, 130−135.
(27) Mu, K.; Si, T.; Li, E.; Xu, R. X.; Ding, H. Numerical study on droplet generation in axisymmetric flow focusing upon actuation. *Phys. Fluids* **2018**, *30* (1), 012111.
(28) Zhang, L.; Ku, T.; Jia, J.; Cheng, X. The role of wettability of nonideal nozzle plate: From drop-on-demand droplet jetting to impact on solid substrate. *AIChE J.* **2018**, *64* (7), 2837−2850.

https://doi.org/10.1021/acs.iecr.4c02237
Ind. Eng. Chem. Res. 2024, 63, 16915−16927